OPEN ACCESS
JOURNAL OF ADVANCED DIELECTRICS
Vol. 13, No. 6 (2023) 2350018 (10 pages)

DOI: 10.1142/S2010135X23500182

Investigation of lead-free $BiFeO_3$–$BaTiO_3$ piezoelectric ceramics through precise composition control

Hailan Qin[*,†], Jianwei Zhao[†,§,**], Xiaoxin Chen[*,†], Hongtian Li[*,†], Shenghao Wang[†], Yuxiao Du[†], Peifeng Li[†], Huanfu Zhou[*,¶,**] and Dawei Wang[‡,‖,**]

[*]*Key Laboratory of Nonferrous Materials and New Processing Technology*
Ministry of Education, College of Materials Science and Engineering
Guilin University of Technology, Guilin 541004, P. R. China

[†]*Shenzhen Institute of Advanced Electronic Materials*
Shenzhen Institute of Advanced Technology
Chinese Academy of Sciences, Shenzhen 518055, P. R. China

[‡]*Functional Materials and Acousto-Optic Instruments Institute*
School of Instrumentation Science and Engineering
Harbin Institute of Technology, Harbin 150080, P. R. China

[§]jianweizhao1106@gmail.com
[¶]zhouhuanfu@163.com
[‖]wangdawei102@gmail.com

Received 25 July 2023; Revised 22 August 2023; Accepted 25 August 2023; Published 26 September 2023

$BiFeO_3$–$BaTiO_3$ is a promising lead-free piezoelectric ceramic, exhibiting high Curie temperature and superior electrochemical characteristics. In this work, $(1-x)BiFeO_3$–$xBaTiO_3$ (BF–xBT, $x = 0.26, 0.28, 0.30, 0.32, 0.34, 0.36$) ceramics were fabricated using the conventional solid-state reaction method through precise composition control. Multiple characterization techniques, including X-ray powder diffraction (XRD), scanning electron microscope (SEM), and electrical property testing systems, were applied to systematically examine the crystallographic structure, microstructure, as well as the dielectric, ferroelectric and piezoelectric properties of the BF–xBT ceramics. The XRD results confirm that all compositions exhibit a typical perovskite structure, transitioning from a single rhombohedral phase to a rhombohedral–cubic phase mixture as the BT content increases. SEM shows apparent core–shell microstructures in the ceramics. Notably, the results demonstrated that the BF–0.30BT ceramic exhibits the maximum piezoelectric constant (d_{33}) ~ 217 pC/N, while the BF–0.34BT ceramic displays the maximum converse piezoelectric constant (d^*_{33}) ~ 323 pm/V, which highlights the suitability of BF–BT ceramics for high-performance piezoelectric applications.

Keywords: $BiFeO_3$–$BaTiO_3$; morphotropic phase boundary; core–shell microstructure; piezoelectricity.

1. Introduction

Piezoelectric ceramics possessing high Curie temperatures (T_C) and outstanding ferroelectric and piezoelectric properties hold immense research significance to meet the growing demand for novel piezoelectric ceramics.[1–3] Although lead-based piezoelectric ceramics have been extensively employed in commercial applications over an extended period, the increasing number of environmentally conscious societies has shed light on their detrimental impact on both human health and the environment. Therefore, the prominence of lead-free piezoelectric ceramics is escalating as a viable alternative.[4–8]

$BiFeO_3$ (BF) is a promising multiferroic material exhibiting a rhombohedral perovskite structure (ABO_3) crystals at room temperature. The high T_C (830°C) and superior theoretical spontaneous polarization ($P_s = 90$–$100\ \mu C/cm^2$) make BF highly interesting for various applications.[9–13] However, the high temperature synthesis process is usually accompanied by the formation of impurity phases like $Bi_2Fe_4O_9$ and $Bi_{25}FeO_{40}$, leading to heterogenous chemical compositions. Moreover, the volatility of bismuth (Bi) and the unstable valence of iron (Fe) contribute to low electrical resistance, high leakage current, and unsaturated ferroelectric hysteresis loops.[9,11,14–17] Therefore, synthesizing high-quality pure-phase BF ceramics independently has been a crucial challenge. It has been found that incorporating different ABO_3 parts into the BF matrix can effectively suppress the generation of heterogeneous phases and enhance electrical resistivity.[18–20] Inspired by the concept of morphotropic phase boundary (MPB) in PZT-based ceramics, researchers have explored ABO_3 materials with distinct crystallographic phases as alternatives to BF for constructing the MPB regions.[21–23] Notably, the incorporation of $BaTiO_3$ (BT)

[**]Corresponding authors.

Table 1. Summary of energy storage and piezoelectric properties of BF-based ceramics.

Composition	Energy storage density (J/cm^3)	d_{33} or d^*_{33}	Reference
0.5BF–0.4ST–0.1BMN–0.03Nb	8.2		30
0.57BF–0.33BT–0.10NN	8.12		31
0.43BF–0.45ST–0.12BT	7.3		32
0.94(0.60BF–0.40BT)–0.06NZN	5.6		33
0.60(0.67BF–0.33BT)–0.40CT	5.03		34
$0.7(B_{0.85}S_{0.15}F)$–0.3BT	4.5		35
0.63(0.87BF)–0.37BT–0.13BZNT	4.85		36
$0.7(B_{0.97}N_{0.03})[F_{0.95}(L_{0.5}N_{0.5})_{0.05}]$–0.3BT	3.2		37
0.65BF–0.33BT–0.02BCZ		640 pm/V	38
BF–BT–BZN		180 pC/N/424 pm/V	39
BF–BT–BMN		148 pC/N/544 pm/V	40
BFS–BT–BZH		180 pC/N/433 pm/V	41
0.67BF–0.33BST		436 pC/N/550 pm/V	42
0.67BF–0.33BTN		400 pm/V	43
0.985(0.67BF–0.33BT)–0.015LN		440 pm/V	44
0.65BF–0.33BT–0.02KNT		433 pm/V	45
BF–BT–CH		95 pC/N/290 pm/V	46

component yields pronounced effects.[24] The BF–BT solid solutions can be formed with delicate chemical composition control. Specifically, as increase the BT content, a phase transition occurs from a ferroelectric (rhombohedral) phase to a paraelectric (cubic) phase across the MPB region, where the dielectric, piezoelectric, and ferroelectric properties can be highly improved.[1,18,22,25–27] However, the research on the MPB composition of BF–BT system is not sufficient. Take the BF–0.30BT composition for instance, numerous reports claimed the best piezoelectric property were varied, namely 134, 225, and 191 pC/N.[23,28,29] Apart from the piezoelectric property, the energy storage properties of BF-based ceramics have also been extensively studied, and recently reported BF-based ceramics with good energy storage and piezoelectric properties are summarized in Table 1.

Based on the aforementioned studies, it is noteworthy that there is a lack of comprehensive and systematic studies reporting the microstructure and properties of BF–xBT ceramics near the MPB region. Therefore, this study aims to address this research gap by preparing BF–xBT ceramics and comparing their properties. In particular, we concentrated on comprehending the impact of BT content on the crystallography, microstructure, dielectric, ferroelectric, piezoelectric and impedance properties of the BF–xBT ceramics.

2. Experimental

BF–xBT ($x = 0.26$, 0.28, 0.30, 0.32, 0.34, 0.36) lead-free ceramics were synthesized using a solid-state reaction method. The chemicals of Bi_2O_3 (99%, Sinopharm, China), $BaCO_3$ (99%, Sinopharm, China), TiO_2 (98%, Sinopharm, China) and Fe_2O_3 (99.9%, Aladdin, China) were used as the raw materials. An excess of 1 mol.% Bi_2O_3 was added to compensate for its volatilization during the sintering process. All chemicals were weighed according to the stoichiometric ratio and wet mixed through a milling process using zirconia balls in ethanol for 24 h. After drying at 80°C, the mixed slurry was calcined at 750°C for 2 h in a sealed alumina crucible, followed by a secondary ball-milling process for 12 h. Then, the calcined powders were mixed with 10 wt.% polyvinyl alcohol (PVA) binder and pressed into 10 mm diameter green pellets under a pressure of 127 MPa for 20 s. The green pellets were stacked on a zirconate plate, covered with alumina crucibles and exposed to a temperature of 600°C for 2 h to remove the PVA, followed by sintering at 1010–1040°C for 3 h. Silver paste was printed on both ceramic surfaces and fired at 850°C for 30 min to form electrodes.

The crystal structure was probed by using the X-ray powder diffraction (XRD, D8 Advance X, Bruker, Germany) with the Cu-K_α radiation. The ceramic surface morphology and element distributions were determined via scanning electron microscope (SEM, Apreo 2, Thermo Scientific, United States) equipped with an energy-dispersive spectroscopy (EDS) detector. The dielectric property and impedance spectroscopy were measured through a precision LCR meter (E4980A, Agilent Technologies, United States) combined with a temperature control system (DMS-1000, Partulab, China). The ferroelectric hysteresis (P–E) loops and field-induced strains (S–E) curves were explored by employing a ferroelectric test system (PK-10E, PolyK Technologies, United States). The piezoelectric constants (d_{33}) were measured by a quasi-static d_{33} meter (SA1303A, PolyK Technologies, United States).

3. Results and Discussion

The XRD patterns of BF–xBT ceramics are shown in Fig. 1(a), revealing the typical perovskite structure for all

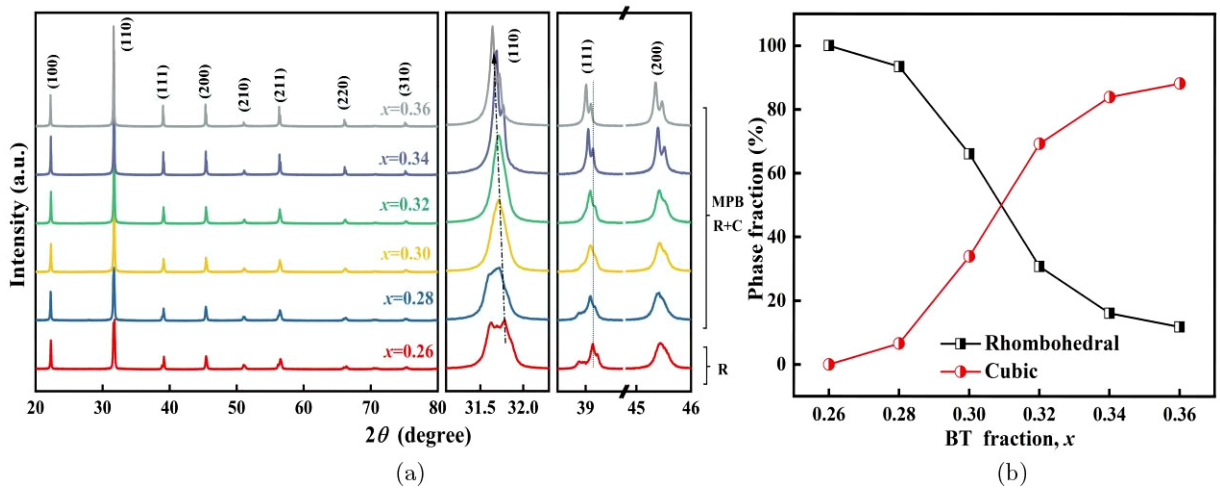

Fig. 1. (a) XRD patterns of BF–xBT ceramics, (b) phase fraction as a function of x.

ceramics. The phase structure of all compositions can be characterized as a pseudo-cubic phase. In the composition of $x = 0.26$, peak splits were observed in (110) and (111), indicating that the ceramic possesses a rhombohedral phase with the space group $R3c$. With increasing the BT content, the peak splits gradually merge into a single peak at (110) and (111), which suggests a rhombohedral–cubic phases mixture, thereby indicating phase transitions occur. Furthermore, all diffraction peaks are shifted toward lower 2θ angles as the BT content increases which evidences an expansion of lattice parameters. The radii of Bi^{3+}, Fe^{3+}, Ba^{2+} and Ti^{4+} ions are 1.03, 0.64, 1.34 and 0.605 Å, respectively.[47] The difference between Fe^{3+} and Ti^{4+} ionic radii are relatively small, whereas Ba^{2+} has a radius $\sim 30\%$ larger than that of Bi^{3+}, leading to the expansion of the volume and cell parameters of the pseudo-cubic unit. The calculated fractions are plotted in Fig. 1(b), illustrating a gradual decrease in the rhombohedral phase fraction and an increase in the cubic phase while

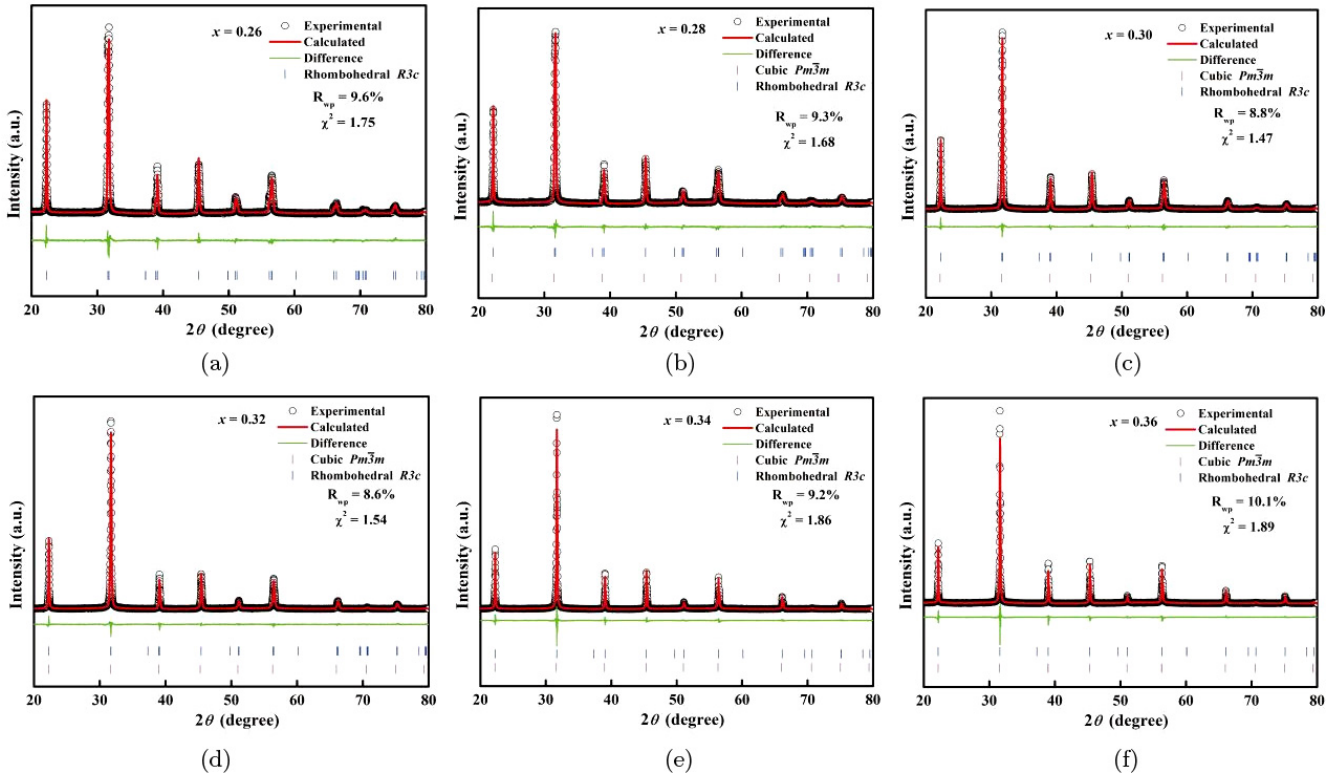

Fig. 2. Rietveld refinement results for BF–xBT ceramics of (a) $x = 0.26$, (b) $x = 0.28$, (c) $x = 0.30$, (d) $x = 0.32$, (e) $x = 0.34$ and (f) $x = 0.36$.

Table 2. The Rietveld refinement results for BF–xBT ceramics.

	Phase fraction (%)		Rhombohedral				Cubic			
x	Rhombohedral ($R3c$)	Cubic ($Pm\bar{3}m$)	a (Å)	b (Å)	c (Å)	V (Å^3)	a (Å)	b (Å)	c (Å)	V (Å^3)
0.26	100	0	5.6276	5.6276	13.8902	380.965	—	—	—	—
0.28	93.4	6.6	5.6328	5.6328	13.8797	381.378	4.0108	4.0108	4.0108	64.521
0.30	66.1	33.9	5.6393	5.6393	13.8590	381.689	4.0045	4.0045	4.0045	64.218
0.32	30.8	69.2	5.6435	5.6435	13.8532	382.105	4.0037	4.0037	4.0037	64.177
0.34	16.1	83.9	5.6517	5.6517	13.8433	382.932	4.0010	4.0010	4.0010	64.047
0.36	11.8	88.2	5.6509	5.6509	13.8421	382.798	3.9990	3.9990	3.9990	63.952

enriching BT content. Rietveld refinement was performed for all compositions, as shown in Fig. 2 and Table 2.

Figure 3 displays the SEM images of the surface morphology of BF–xBT ceramics. All samples exhibit clear grain boundaries that are relatively homogeneous, nearly free of pores and relatively dense. The relative density of a specific composition was calculated based on the theoretical density obtained from the XRD refinement and the actual bulk density measured via the Archimedes method. All ceramics present a relative density larger than 95% that is supported by the SEM results. Statistical analysis reveals that the average grain size is composition-dependent, which tends to increase and then decrease with the increase of x content. Specifically, the maximum grain size of $\sim 9.82\,\mu$m is achieved at $x = 0.34$.

Figures 4(a)–4(f) provide the backscattered electron (BSE) images of the fine-polished BF–xBT ceramic surfaces, revealing the presence of core–shell microstructures for all compositions. A distinct contrast between light and dark regions can be observed, with the core appearing brighter due to the enrichment of Bi and Fe elements, while the shell appears relatively darker because of the abundance of Ba and Ti elements. Figures 4(g)–4(l) present the heterogeneous element distributions surrounding a core–shell microstructure

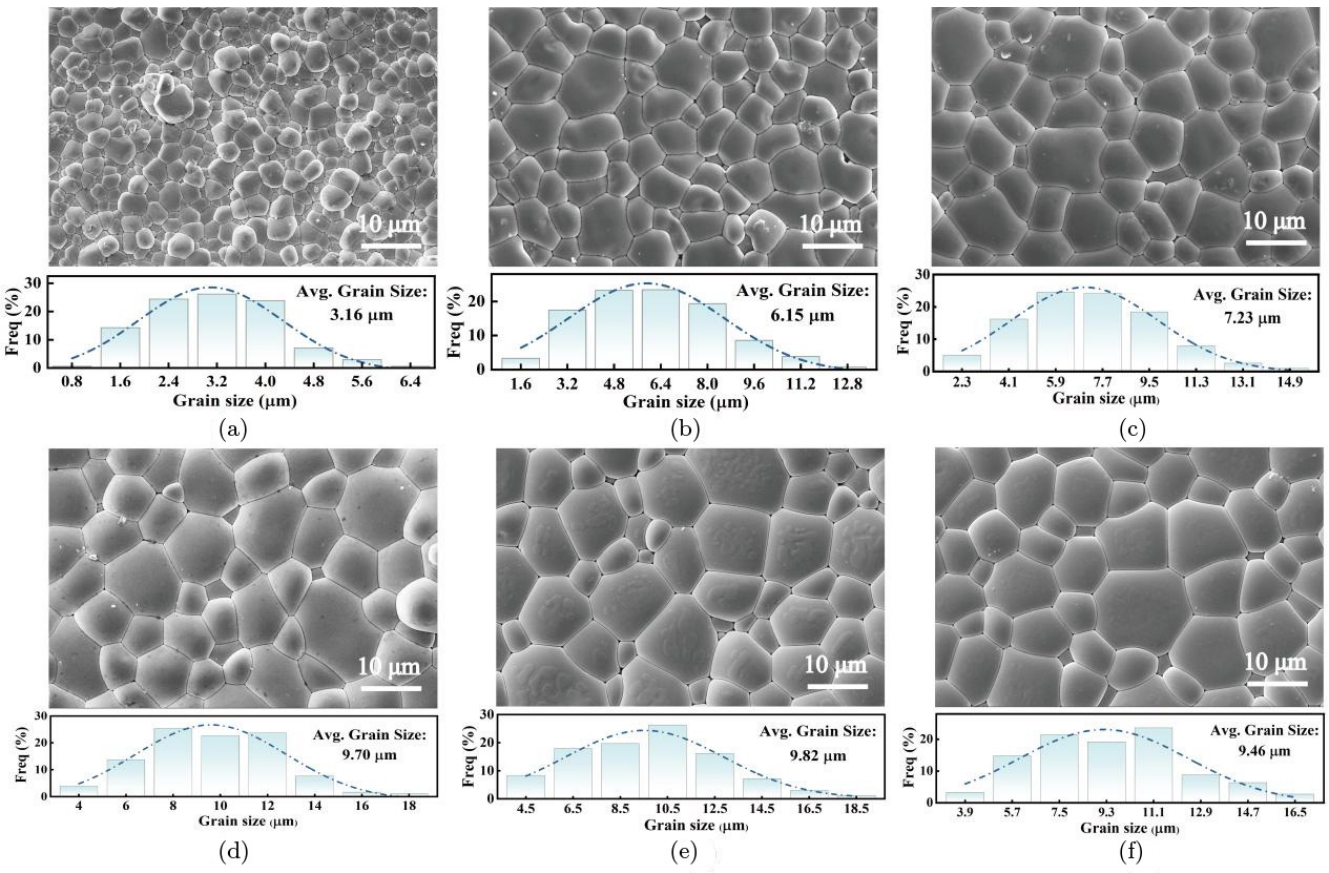

Fig. 3. The surface morphology and grain size distribution of the BF–xBT ceramics with (a) $x = 0.26$, (b) $x = 0.28$, (c) $x = 0.30$, (d) $x = 0.32$, (e) $x = 0.34$ and (f) $x = 0.36$.

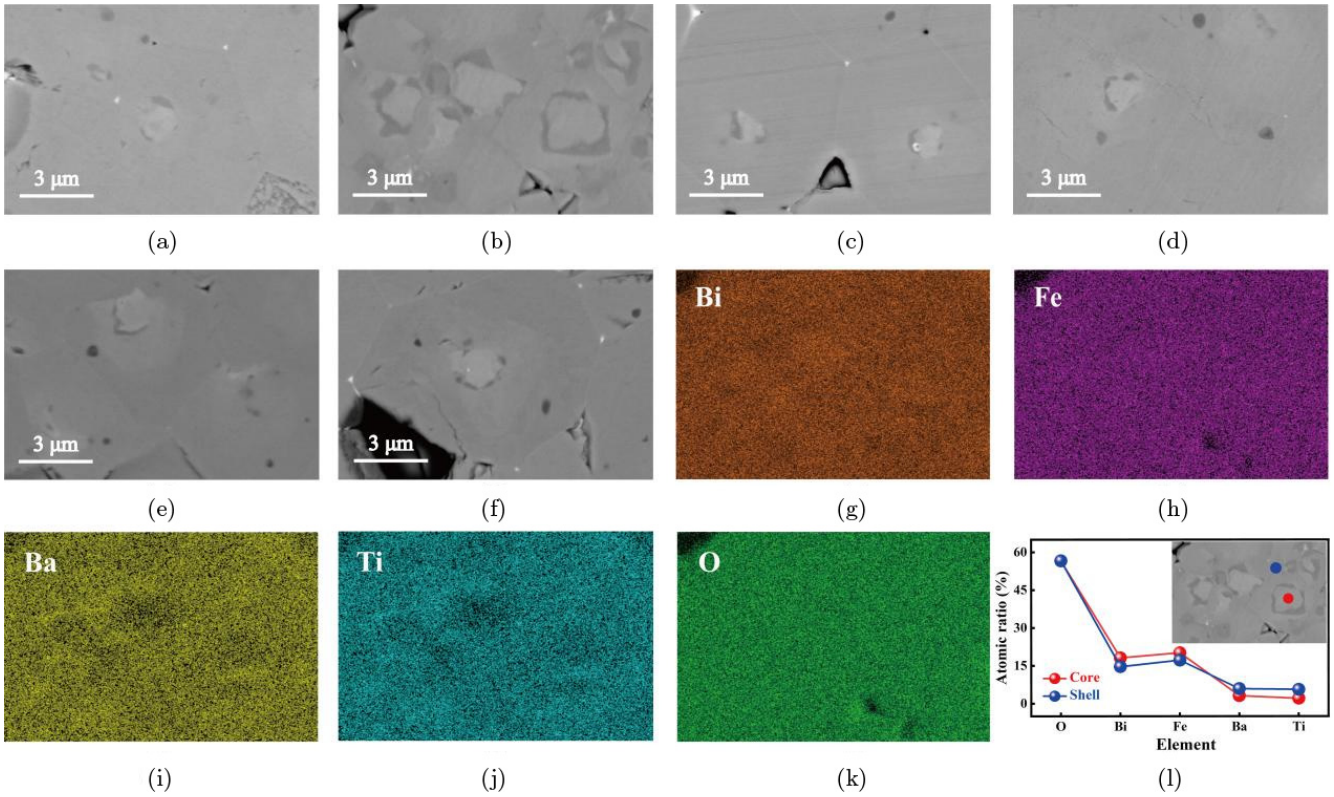

Fig. 4. BSE images of polished surfaces of BF–xBT ceramics with (a) $x = 0.26$, (b) $x = 0.28$, (c) $x = 0.30$, (d) $x = 0.32$, (e) $x = 0.34$ and (f) $x = 0.36$; EDS elemental mapping results of the representative BF–0.28BT with (g) Bi, (h) Fe, (i) Ba, (j) Ti, (k) O, (l) EDS point data of BF–0.28BT.

for a representative composition, $x = 0.28$. The core–shell microstructure is believed to be arisen the microscopic segregation of elements during the slow cooling process of sintering.[39,40,48–50]

The temperature-dependent relative permittivity (ε_r) and dielectric loss ($\tan\delta$) at a frequency of 10 kHz are depicted in Fig. 5(a). The figure reveals that the dielectric peak gradually broadens, indicating a diffusive phase transition and a gradual shift toward relaxor ferroelectrics. In addition, the $\tan\delta$ exhibits a rapid increase around the T_m, which is mainly due to the sharp increase of conductivity at high temperature. The plots show asymmetric shapes in the dielectric peaks, which is related to the presence of core–shell structures within the ceramics (Fig. 4). Figure 5(b) shows the T_m corresponding to different BT contents. It illustrates that T_m decreases from 567°C at $x = 0.26$ to 389°C at $x = 0.36$, which is due to the

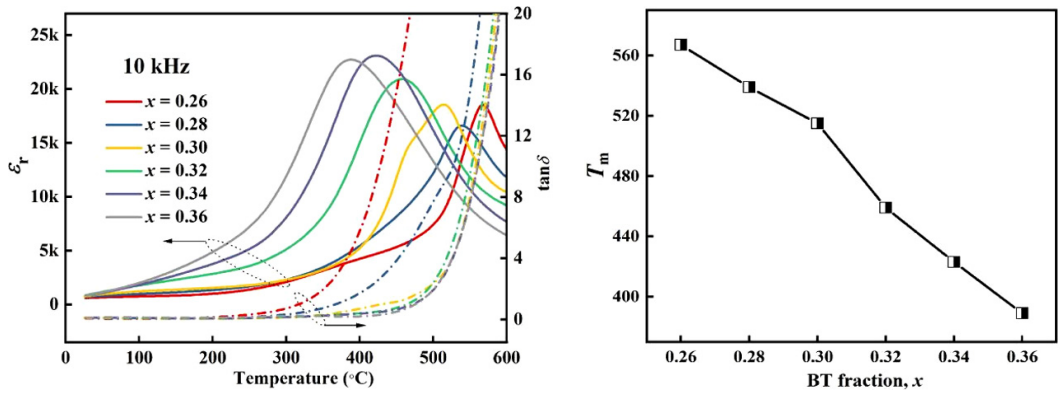

Fig. 5. (a) Temperature-dependent ε_r and $\tan\delta$ measured at 10 kHz, (b) the T_m at 10 kHz, (c) the γ at 10 kHz, (d) the ΔT_m from 1 kHz to 1 MHz.

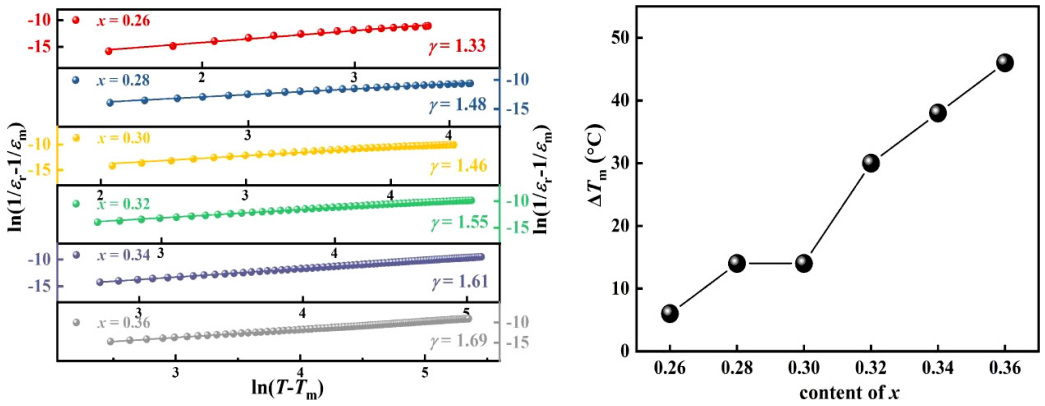

(c) (d)

Fig. 5. (*Continued*)

lower $T_C = (120^\circ\text{C})$ in the pure BT.[24] The relaxor ferroelectric behavior of BF–xBT ceramics could be characterized by the relaxation coefficient (γ) and the T_m difference (ΔT_m) at various frequencies, as plotted in Figs. 5(c) and 5(d). It can be observed that the values of both γ and ΔT_m increase with increasing the BT content, indicating a gradual relaxation of the BF–xBT ceramics, corresponding to the observations in Fig. 5(a). The plots of temperature-dependent of ε_r and $\tan\delta$ of each composition at different frequencies are shown in Fig. 6.

The impedance complex plane (Z^*) plots of BF–xBT ceramics at 400°C are shown in Fig. 7(a), where Z' and Z'' represent the real and the imaginary parts of Z^*, respectively. At the temperature of 400°C, the semicircle progressively enlarges as the BT content increases, indicating an enhancement in the total resistivity. The shape of the semicircle deviates from the regular shape, indicating that there are at least two electroactive components at high temperature.[30] The Z'' and M''/ε_0 plots of $x = 0.34$ are depicted in Fig. 7(b), spotlighting the electrical heterogeneity is related to various electroactive components. Three peaks are found in the plots corresponding to the three electroactive components. At the lower frequency area, the peaks at Z'' and M''/ε_0 correspond to the grain boundary response (component 1) and shell

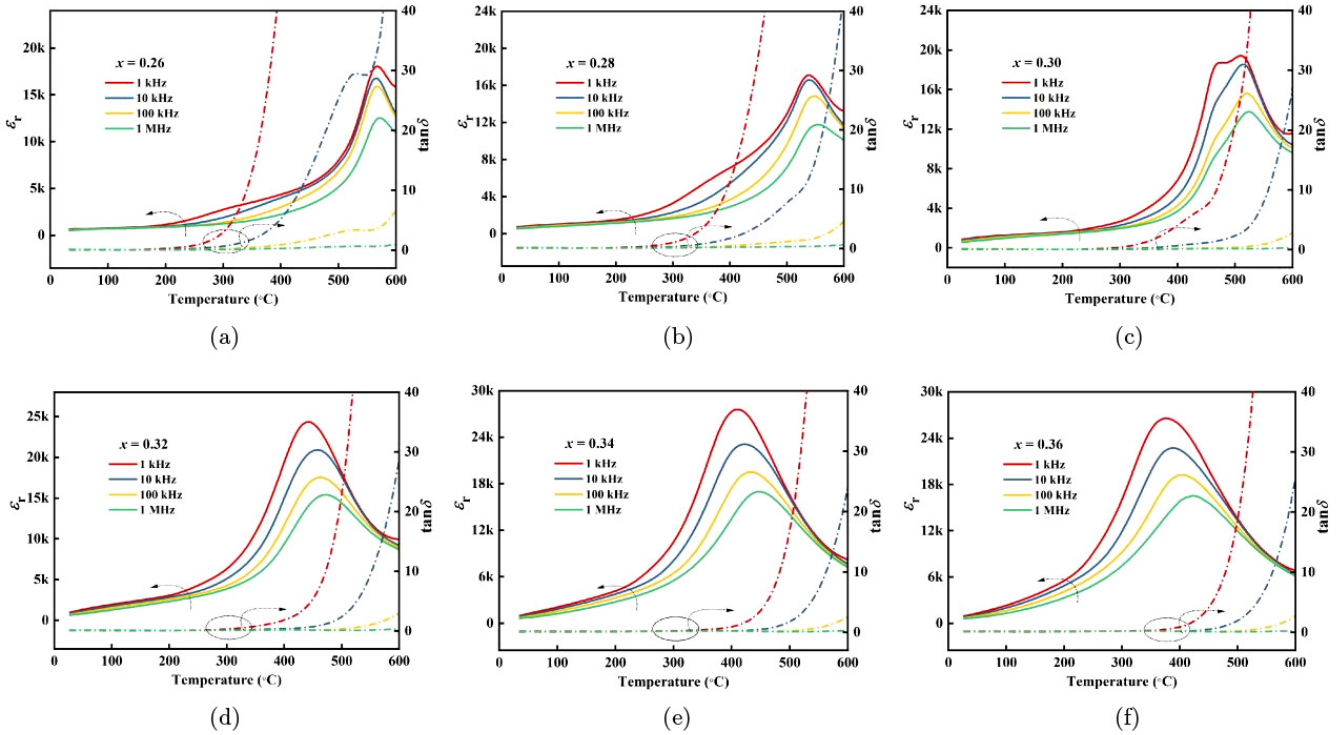

(a) (b) (c)

(d) (e) (f)

Fig. 6. Temperature-dependent ε_r and $\tan\delta$ measured at different frequencies of 1, 10, 100 kHz and 1 MHz for the BF–xBT ceramics with (a) $x = 0.26$, (b) $x = 0.28$, (c) $x = 0.30$, (d) $x = 0.32$, (e) $x = 0.34$ and (f) $x = 0.36$.

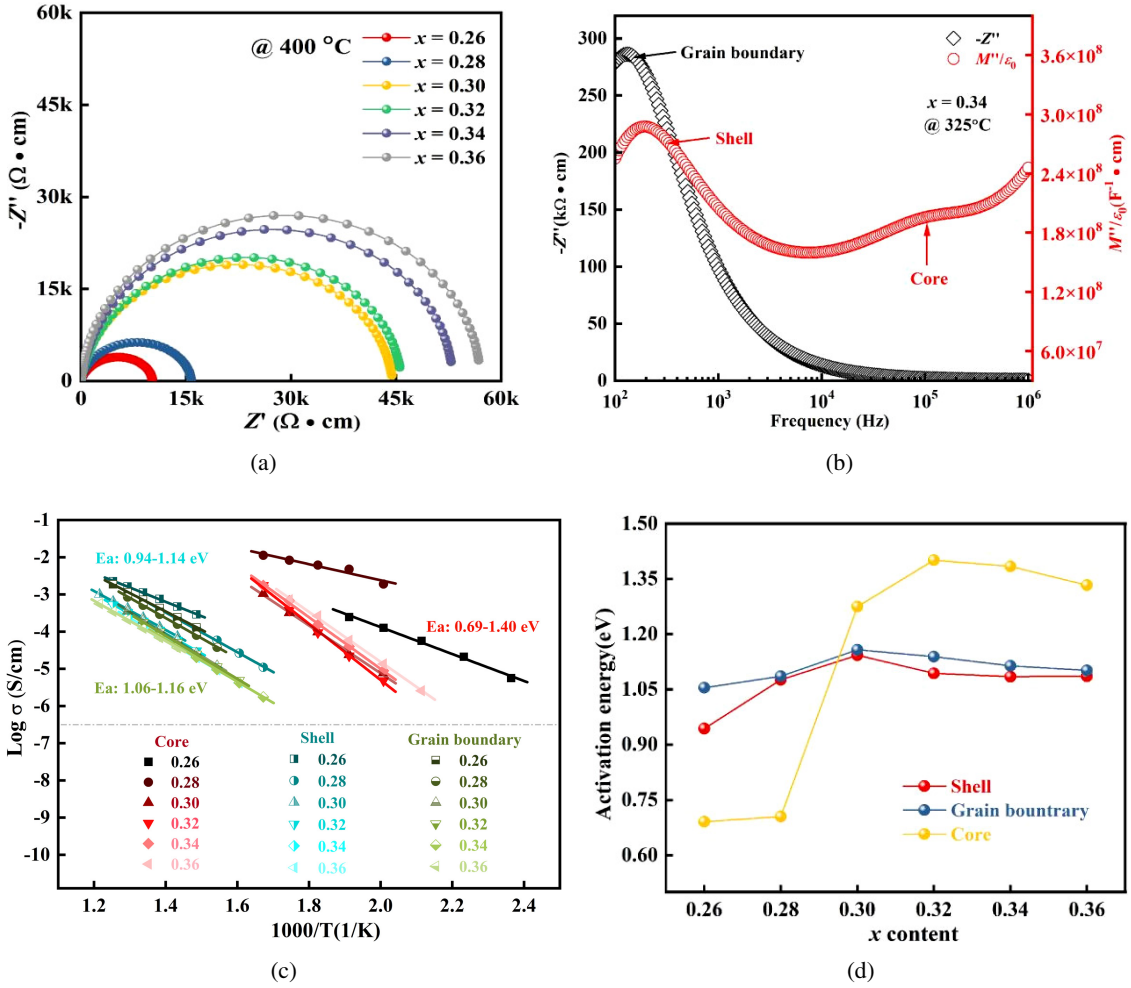

Fig. 7. (a) Temperature-dependent Z^* plots for BF–xBT ceramics at 400°C, (b) combined Z'' and M''/ε_0 spectroscopic plots at 325°C for $x = 0.34$, (c) Arrhenius plots, and (d) the calculated activation energies for the BF–xBT ceramics.

response (component 2), respectively, whereas the peaks in the higher frequency region of the M''/ε_0 are considered as the core response (component 3), which is mainly attributed to the electrical heterogeneity characterized by the core–shell structure, a phenomenon that is observed in all components. The data can be analyzed using an equivalent circuit model of three parallel resistor–capacitor elements connected in series, and the resistance (R) and capacitance (C) of these components were calculated based on the peaks of Z'' and M''/ε_0 shown in Table 3. The R values of components 1 and 2 increase with increasing the BT content, while component 3 barely changes as the BT content. Figure 7(c) shows the Arrhenius plots of the grain shell, core and boundary, and the activation energy calculated by fitting is shown in Fig. 7(d).

Table 3. The values of R and C for each conductive component at 325°C derived from the Z'' and M''/ε_0 peak values for BF–xBT ceramics.

	Component 1 (Grain boundary)		Component 2 (Shell)		Component 3 (Core)	
Composition	$R = 2Z''$ (kΩ·cm)	$C = 1/(4\pi f Z'')$ (F cm^{-1})	$R = M''/(\varepsilon_0 \pi f)$ (kΩ·cm)	$C = \varepsilon_0/(2M'')$ (F cm^{-1})	$R = M''/(\varepsilon_0 \pi f)$ (kΩ·cm)	$C = \varepsilon_0/(2M'')$ (F cm^{-1})
0.26 (325°C)	78	4.81×10^{-10}	30	2.51×10^{-10}	0.96	3.48×10^{-10}
0.28 (325°C)	146	4.28×10^{-10}	91	2.84×10^{-10}	0.28	1.18×10^{-9}
0.30 (325°C)	474	3.48×10^{-10}	378	2.88×10^{-10}	0.95	1.06×10^{-9}
0.32 (325°C)	509	1.30×10^{-9}	378	1.00×10^{-9}	0.58	1.93×10^{-9}
0.34 (325°C)	572	2.11×10^{-9}	479	1.74×10^{-9}	0.58	2.55×10^{-9}
0.36 (325°C)	627	2.21×10^{-9}	559	1.97×10^{-9}	0.44	3.50×10^{-9}

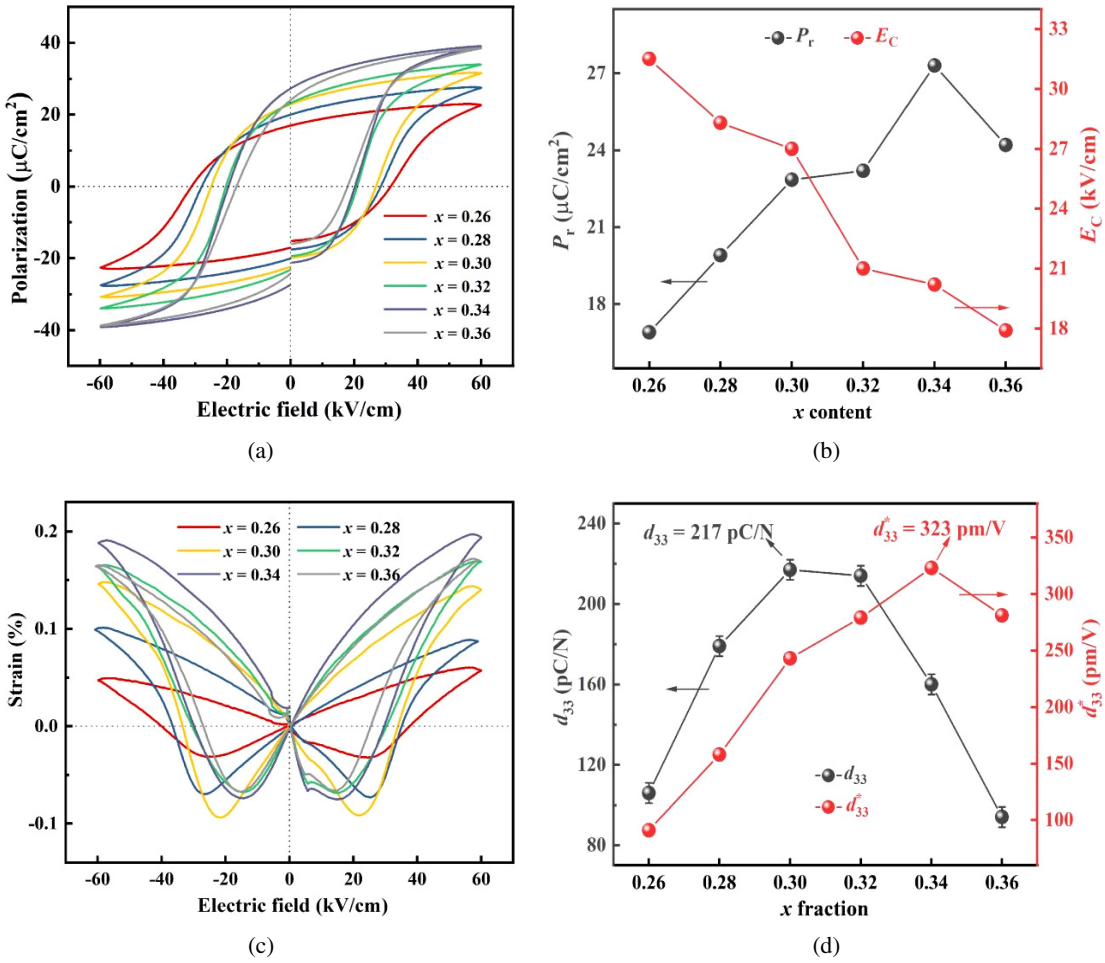

Fig. 8. (a) P–E loops at 60 kV/cm, and associated (b) P_r and E_C for the BF–xBT ceramics; (c) S–E curves at 60 kV/cm, and (d) d_{33} and d^*_{33} as a function of x for the BF–xBT ceramics.

The activation energy of the cores (0.69–1.40 eV) fluctuates a lot, while that of the grain boundaries (1.06–1.16 eV) are all slightly higher than those of the shells (0.94–1.14 eV). However, it is noteworthy that the resistivity of shell and grain boundary exceeds that of the core for 2–3 orders of magnitude.

Figure 8(a) presents the P–E loops of the BF–xBT ceramics under an electric field of 60 kV/cm and a frequency of 1 Hz at room temperature. All compositions exhibit a saturated P–E loop which is a indicative behavior of typical ferroelectric behavior. The corresponding remanent polarization (P_r) and coercive field (E_C) of the P–E loops are summarized in Fig. 8(b). With increasing the BT content, the E_C changes from 31.5 kV/cm at $x = 0.26$ to 17.9 kV/cm at $x = 0.36$. The P_r initially increases from 16.9 μC/cm^2 at $x = 0.26$ to 27.3 μC/cm^2 at $x = 0.34$ and then decreases to 24.2 μC/cm^2 at $x = 0.36$. Figure 8(c) shows the S–E curves for ceramics measured at 60 kV/cm, and all curves exhibit a typical butterfly shape. The strain value is found to increase as the x increases from 0.26 to 0.34, reaching a maximum value of 0.194% at $x = 0.34$, which is attributed to the multiple local symmetries proposed by Wang *et al.* and Lu *et al.*[25–27] Both the d_{33} and d^*_{33} values exhibit an initial increase followed by a decrease, as plotted in Fig. 8(d). The measured d_{33} values reach a maximum of 217 pC/N at $x = 0.30$ with increasing BT content. Beyond that point, they decrease as BT content increases. This behavior is attributed to the phase structure at $x = 0.30$ being located at the MPB with 66% of the rhombohedral phase and the absence of any impurity phases, resulting in readily domain switching and polarization rotation with applied electric fields.

4. Conclusions

This study employed precise composition control to investigate the evolution of structure, morphology, and electrical properties in BF–xBT lead-free ceramics near the MPB region. The examination encompassed the phase structure, microstructure, impedance, dielectric, ferroelectric, and piezoelectric properties. XRD analysis reveals a transition from a single rhombohedral phase to the coexistence of cubic phases with increasing the BT content. SEM images indicate

an initial increase and subsequent decrease in grain size as the BT content increases, reaching a peak at $x = 0.34$. The presence of microscopic core–shell structures has been observed in all compositions. As the BT content increases, the ceramics gradually show stronger behaviors of relaxor ferroelectrics, with an overall increase in electrical resistivity. The E_C tends to decrease, while the P_r initially increases and then decreases, reaching a maximum value of 27.3 μC/cm^2 at $x = 0.34$. The highest $d_{33} \sim 217$ pC/N and $d^*_{33} \sim 323$ pm/V are achieved at $x = 0.30$ and $x = 0.34$, respectively. To summarize, this study provides valuable insights on the composition-dependent changes in structure and properties in the BF–xBT ceramics near the MPB, which serves as a foundation for further research and exploration of the lead-free piezoelectric materials.

Acknowledgments

This work is supported by the Science, Technology and Innovation Committee of Shenzhen Municipality (Grant Nos.: JCYJ20220531095802005 and RCBS20210706092341001).

References

[1]D. Wang, G. Wang, S. Murakami, Z. Fan, A. Feteira, D. Zhou, S. Sun, Q. Zhao and I. M. Reaney, $BiFeO_3$–$BaTiO_3$: A new generation of lead-free electroceramics, *J. Adv. Dielectr.* **8**, 1830004 (2018).

[2]J. Rödel, K. G. Webber, R. Dittmer, W. Jo, M. Kimura and D. Damjanovic, Transferring lead-free piezoelectric ceramics into application, *J. Eur. Ceram. Soc.* **35**, 1659 (2015).

[3]Y. Saito, H. Takao, T. Tani, T. Nonoyama, K. Takatori, T. Homma, T. Nagaya and M. Nakamura, Lead-free piezoceramics, *Nature* **432**, 84 (2004).

[4]C.-H. Hong, H.-P. Kim, B.-Y. Choi, H.-S. Han, J. S. Son, C. W. Ahn and W. Jo, Lead-free piezoceramics — where to move on? *J. Mater.* **2**, 1 (2015).

[5]P. K. Panda and B. Sahoo, PZT to lead free piezo ceramics: A review, *Ferroelectrics* **474**, 128 (2015).

[6]E. Cross, Materials science: Lead-free at last, *Nature* **432**, 24 (2004).

[7]J. de Souza-Araujo, N. E. Hussey, R. A. Hauser-Davis, A. H. Rosa, M. de Oliveira Lima and T. Giarrizzo, Human risk assessment of toxic elements (As, Cd, Hg, Pb) in marine fish from the Amazon, *Chemosphere* **301**, 134575 (2022).

[8]M. J. McFarland, M. E. Hauer and A. Reuben, Half of US population exposed to adverse lead levels in early childhood, *Proc. Natl. Acad. Sci. USA* **119**, e2118631119 (2022).

[9]J. Wang, J. B. Neaton, H. Zheng, V. Nagarajan, S. B. Ogale, B. Liu, D. Viehland, V. Vaithyanathan, D. G. Schlom, U. V. Waghmare, N. A. Spaldin, K. M. Rabe, M. Wuttig and R. Ramesh, Epitaxial $BiFeO_3$ multiferroic thin film heterostructures, *Science* **299**, 1719 (2003).

[10]N. Hur, S. Park, P. A. Sharma, J. S. Ahn, S. Guha and S.-W. Cheong, Electric polarization reversal and memory in a multiferroic material induced by magnetic fields, *Nature* **429**, 392 (2004).

[11]T. Rojac, M. Kosec, B. Budic, N. Setter and D. Damjanovic, Strong ferroelectric domain-wall pinning in $BiFeO_3$ ceramics, *J. Appl. Phys.* **108**, 074107 (2010).

[12]Z.-J. Li, Z.-L. Hou, W.-L. Song, X.-D. Liu, D.-W. Wang, J. Tang and X.-H. Shao, Mg-substitution for promoting magnetic and ferroelectric properties of $BiFeO_3$ multiferroic nanoparticles, *Mater. Lett.* **175**, 207 (2016).

[13]D. Wang, M. Wang, F. Liu, Y. Cui, Q. Zhao, H. Sun, H. Jin and M. Cao, Sol–gel synthesis of Nd-doped $BiFeO_3$ multiferroic and its characterization, *Ceram. Int.* **41**, 8768 (2015).

[14]G. Catalan and J. F. Scott, Physics and applications of bismuth ferrite, *Adv. Mater.* **21**, 2463 (2009).

[15]T. Rojac, A. Bencan, B. Malic, G. Tutuncu, J. L. Jones, J. E. Daniels and D. Damjanovic, $BiFeO_3$ ceramics: Processing, electrical, and electromechanical properties, *J. Am. Ceram. Soc.* **97**, 1993 (2014).

[16]G.-Y. Zhang, J.-Q. Dai and Y.-S. Lu, Phase structure and electrical properties of $(1-x)Bi_{1+y}FeO_3$–$x$$BaTiO_3$ lead-free ceramics with different Bi contents, *J. Mater. Sci.: Mater. Electron.* **32**, 10289 (2021).

[17]W. Yi, Z. Lu, X. Liu, D. Huang, Z. Jia, Z. Chen, X. Wang and H. Zhu, Excellent piezoelectric performance of Bi-compensated $0.69BiFeO_3$–$0.31BaTiO_3$ lead-free piezoceramics, *J. Mater. Sci.: Mater. Electron.* **32**, 22637 (2021).

[18]M. Mahesh Kumar, A. Srinivas and S. V. Suryanarayana, Structure property relations in $BiFeO_3$/$BaTiO_3$ solid solutions, *J. Appl. Phys.* **87**, 855 (2000).

[19]Y. Shi, F. Yan, X. He, K. Zhu, G. Li, X. Dong, B. Shen and J. Zhai, Performances variations of $BiFeO_3$-based ceramics induced by additives with diverse phase structures, *CrystEngComm* **23**, 1596 (2021).

[20]S. A. Khan, F. Akram, J. Bae, T. Ahmed, T. K. Song, Y. S. Sung, M.-H. Kim and S. Lee, Enhancing piezoelectric coefficient with high Curie temperature in $BiAlO_3$-modified $BiFeO_3$–$BaTiO_3$ lead-free ceramics, *Solid State Sci.* **98**, 106040 (2019).

[21]J. Wu, Z. Fan, D. Xiao, J. Zhu and J. Wang, Multiferroic bismuth ferrite-based materials for multifunctional applications: Ceramic bulks, thin films and nanostructures, *Prog. Mater. Sci.* **84**, 335 (2016).

[22]S. O. Leontsev and R. E. Eitel, Dielectric and piezoelectric properties in Mn-modified $(1-x)BiFeO_3$–$x$$BaTiO_3$ ceramics, *J. Am. Ceram. Soc.* **92**, 2957 (2009).

[23]Y. Wei, X. Wang, J. Zhu, X. Wang and J. Jia, Dielectric, ferroelectric, and piezoelectric properties of $BiFeO_3$–$BaTiO_3$ ceramics, *J. Am. Ceram. Soc.* **96**, 3163 (2013).

[24]I. H. Ismailzade, R. M. Ismailov, A. I. Alekberov and F. M. Salaev, Investigation of the magnetoelectric $(ME)_H$ effect in solid solutions of the systems $BiFeO_3$–$BaTiO_3$ and $BiFeO_3$–$PbTiO_3$, *Phys. Status Solidi* **68**, k81 (1981).

[25]G. Wang, T. Hu, W. Zhu, Z. Lu, A. Kleppe, M. D. Lopez, A. Feteira, D. C. Sinclair, Z. Fu, H. Huang, D. Wang and I. M. Reaney, Multiple local symmetries result in a common average polar axis in high-strain $BiFeO_3$-based ceramics, *Phys. Rev. Lett.* **130**, 076801 (2023).

[26]Z. Lu, G. Wang, L. Li, Y. Huang, A. Feteira, W. Bao, A. K. Kleppe, F. Xu, D. Wang and I. M. Reaney, *In situ* poling X-ray diffraction studies of lead-free $BiFeO_3$-$SrTiO_3$ ceramics, *Mater. Today Phys.* **19**, 100426 (2021).

[27]G. Wang, Z. Fan, S. Murakami, Z. Lu, D. A. Hall, D. C. Sinclair, A. Feteira, X. Tan, J. L. Jones, A. K. Kleppe, D. Wang and

I. M. Reaneya, Origin of the large electrostrain in $BiFeO_3$–$BaTiO_3$ based lead-free ceramics, *J. Mater. Chem. A* **7**, 21254 (2019).
[28]B. Xun, A. Song, J. Yu, Y. Yin, J.-F. Li and B.-P. Zhang, Lead-free $BiFeO_3$–$BaTiO_3$ ceramics with high curie temperature: Fine compositional tuning across the phase boundary for high piezoelectric charge and strain coefficients, *ACS Appl. Mater. Interfaces* **13**, 4192 (2021).
[29]L.-F. Zhu, B.-P. Zhang, Z.-C. Zhang, S. Li, L.-J. Wang and L.-J. Zheng, Piezoelectric, ferroelectric and ferromagnetic properties of $(1-x)BiFeO_3$–$xBaTiO_3$ lead-free ceramics near morphotropic phase boundary, *J. Mater. Sci.: Mater. Electron.* **29**, 2307 (2017).
[30]Z. Lu, G. Wang, W. Bao, J. Li, L. Li, A. Mostaed, H. Yang, H. Ji, D. Li, A. Feteira, F. Xu, D. C. Sinclair, D. Wang, S.-Y. Liu and I. M. Reaney, Superior energy density through tailored dopant strategies in multilayer ceramic capacitors, *Energy. Environ. Sci.* **13**, 2938 (2020).
[31]H. Qi, A. Xie, A. Tian and R. Zuo, Superior energy-storage capacitors with simultaneously giant energy density and efficiency using nanodomain engineered $BiFeO_3$–$BaTiO_3$–$NaNbO_3$ lead-free bulk ferroelectrics, *Adv. Energy. Mater.* **10**, 1903338 (2019).
[32]T. Cui, A. Yu, Y. Zhang, J. Guo, X. Li, S. Guo, J. Zhang, J. Wang and S.-T. Zhang, Energy storage performance of $BiFeO_3$–$SrTiO_3$–$BaTiO_3$ relaxor ferroelectric ceramics, *J. Am. Ceram. Soc.* **105**, 6252 (2022).
[33]D. Wang, Z. Fan, W. Li, D. Zhou, A. Feteira, G. Wang, S. Murakami, S. Sun, Q. Zhao, X. Tan and I. M. Reaney, High energy storage density in $Nd(Zn_{2/3}Nb_{1/3})O_3$-doped $BiFeO_3$–$BaTiO_3$ ceramics, *Adv. Electron. Mater.* **9**, 2200930 (2022).
[34]W. Ye, C. Zhu, Y. Xiao, X. Bai, P. Zheng, J. Zhang, W. Bai, Q. Fan, L. Zheng and Y. Zhang, Remarkable energy-storage performances and excellent stability in $CaTiO_3$-doped $BiFeO_3$–$BaTiO_3$ relaxor ferroelectric ceramics, *J. Eur. Ceram. Soc.* **43**, 900 (2023).
[35]R. Montecillo, C.-S. Chen, Y.-T. Lee, P.-Y. Chen and C.-S. Tu, Optimized electric-energy storage in $BiFeO_3$–$BaTiO_3$ ceramics via tailoring microstructure and nanocluster, *J. Eur. Ceram. Soc.* **43**, 1941 (2023).
[36]F. Kang, L. Zhang, W. Yang, R. Kang, R. Xue, L. He, Q. Sun, T. Zhang, Z. Wang, J. Wang and K. Zeng, Achieving ultrahigh energy storage performance in $BiFeO_3$–$BaTiO_3$ based lead free relaxors via a composition optimization strategy, *J. Eur. Ceram. Soc.* **42**, 6958 (2022).
[37]A. Khesro, F. A. Khan, R. Muhammad, A. Ali, M. Khan and D. Wang, Energy storage performance of Nd^{3+}-doped $BiFeO_3$–$BaTiO_3$-based lead-free ceramics, *Ceram. Int.* **48**, 29938 (2022).
[38]X. Liu, J. Zhai and B. Shen, Novel bismuth ferrite-based lead-free incipient piezoceramics with high electromechanical response, *J. Mater. Chem. C* **7**, 5122 (2019).
[39]D. Wang, Z. Fan, W. Li, D. Zhou, A. Feteira, G. Wang, S. Murakami, S. Sun, Q. Zhao, X. Tan and I. M. Reaney, High energy storage density and large strain in $Bi(Zn_{2/3}Nb_{1/3})O_3$-doped $BiFeO_3$–$BaTiO_3$ ceramics, *ACS Appl. Energy. Mater.* **1**, 4403 (2018).
[40]S. Murakami, D. Wang, A. Mostaed, A. Khesro, A. Feteira, D. C. Sinclair, Z. Fan, X. Tan, I. M. Reaney, High strain (0.4%) $Bi(Mg_{2/3}Nb_{1/3})O_3$–$BaTiO_3$–$BiFeO_3$ lead-free piezoelectric ceramics and multilayers, *J. Am. Ceram. Soc.* **101**, 5428 (2018).
[41]T. Zheng and J. Wu, Perovskite $BiFeO_3$–$BaTiO_3$ ferroelectrics: Engineering properties by domain evolution and thermal depolarization modification, *Adv. Electron Mater.* **6**, 2000079 (2020).
[42]M. Habib, L. Tang, G. Xue, X. Zhou and D. Zhang, Improvement in piezoelectric performance of the lead-free $BiFeO_3$–$BaTiO_3$ ceramics by synergistic approach, *J. Mater. Sci. Technol.* **160**, 55 (2023).
[43]Q. Iqbal, M. Habib, M. Alzaid, P. Ahmad and M. T. Khan, Synergistic approach for enhancement of piezoelectricity in the lead-free $BiFeO_3$–$BaTiO_3$ ceramics, *J. Alloys Compd.* **947**, 169414 (2023).
[44]R. A. Malik, A. Zaman, A. Hussain, A. Maqbool, T. K. Song, W.-J. Kim, Y. S. Sung and M.-H. Kim, Temperature invariant high dielectric properties over the range 200°C–500°C in $BiFeO_3$ based ceramics, *J. Eur. Ceram. Soc.* **38**, 2259 (2018).
[45]N. Zhao, H. Fan, X. Ren, J. Ma, J. Bao, Y. Guo and Y. Zhou, Dielectric, impedance and piezoelectric properties of $(K_{0.5}Nd_{0.5})$-TiO_3-doped $0.67BiFeO_3$–$0.33BaTiO_3$ ceramics, *J. Eur. Ceram. Soc.* **39**, 4096 (2019).
[46]J. Zhao, H. Qin, X. Chen, S. Yu and D. Wang, Enhanced piezoelectric properties and electrical resistivity in $CaHfO_3$ modified $BiFeO_3$–$BaTiO_3$ lead-free piezoceramics, *J. Mater.* (2019), https://doi.org/10.1016/j.jmat.2023.07.001.
[47]A. A. B. Baloch, S. M. Alqahtani, F. Mumtaz, A. H. Muqaibel, S. N. Rashkeev and F. H. Alharbi, Extending Shannon's ionic radii database using machine learning, *Phys. Rev. Mater.* **5**, 043804 (2021).
[48]I. Calisir and D. A. Hall, Chemical heterogeneity and approaches to its control in $BiFeO_3$–$BaTiO_3$ lead-free ferroelectrics, *J. Mater. Chem. C* **6**, 134 (2018).
[49]S. Murakami, N. T. A. F. Ahmed, D. Wang, A. Feteira, D. C. Sinclair and I. M. Reaney, Optimising dopants and properties in $BiMeO_3$ (Me = Al, Ga, Sc, Y, $Mg_{2/3}Nb_{1/3}$, $Zn_{2/3}Nb_{1/3}$, $Zn_{1/2}Ti_{1/2}$) lead-free $BaTiO_3$–$BiFeO_3$ based ceramics for actuator applications, *J. Eur. Ceram. Soc.* **38**, 4220 (2018).
[50]I. Calisir, A. A. Amirov, A. K. Klepped and D. A. Hall, Optimisation of functional properties in lead-free $BiFeO_3$–$BaTiO_3$ ceramics through La^{3+} substitution strategy, *J. Mater. Chem. A* **6**, 5378 (2018).